AGU PUBLICATIONS

JGR

Journal of Geophysical Research: Space Physics

RESEARCH ARTICLE
10.1002/2017JA024612

Key Points:
- Ring/shell ion distributions with $\partial f_p(v_\perp)/\partial v_\perp > 0$ near $v_{||} = 0$ are commonly found on the dayside of the magnetosphere
- A new method for characterizing distributions is used, allowing analytical moment calculation and linear dispersion analysis
- Ring/shell distributions that are potentially ion Bernstein-unstable are also subject to the Alfvén cyclotron instability

Correspondence to:
M. F. Thomsen,
mthomsen@psi.edu

Citation:
Thomsen, M. F., Denton, M. H., Gary, S. P., Liu, K., & Min, K. (2017). Ring/shell ion distributions at geosynchronous orbit. *Journal of Geophysical Research: Space Physics*, *122*, 12,055–12,071. https://doi.org/10.1002/2017JA024612

Received 21 JUL 2017
Accepted 4 NOV 2017
Accepted article online 8 NOV 2017
Published online 11 DEC 2017

Ring/Shell Ion Distributions at Geosynchronous Orbit

M. F. Thomsen[1], M. H. Denton[2,3], S. P. Gary[3], Kaijun Liu[4], and Kyungguk Min[5]

[1]Planetary Science Institute, Tucson, AZ, USA, [2]New Mexico Consortium, Los Alamos, NM, USA, [3]Center for Space Plasma Physics, Space Science Institute, Boulder, CO, USA, [4]Department of Physics, Auburn University, Auburn, AL, USA, [5]Applied Physics Laboratory, The Johns Hopkins University, Laurel, MD, USA

Abstract One year's worth of plasma observations from geosynchronous orbit is examined for ion distributions that may simultaneously be subject to the ion Bernstein (IB) instability (generating fast magnetosonic waves) and the Alfvén cyclotron (AC) instability (generating electromagnetic ion cyclotron waves). Confirming past analyses, distributions with robust $\partial f_p(v_\perp)/\partial v_\perp > 0$ near $v_{||} = 0$, which we denote as "ring/shell" distributions, are commonly found primarily on the dayside of the magnetosphere. A new approach to high-fidelity representation of the observed ring/shell distribution functions in a form readily suited to both analytical moment calculation and linear dispersion analysis is presented, which allows statistical analysis of the ring/shell properties. The ring/shell temperature anisotropy is found to have a clear upper limit that depends on the parallel beta of the ring/shell ($\beta_{||r}$) in a manner that is diagnostic of the operation of the AC instability. This upper limit is only reached in the postnoon events, which are primarily produced by the energy- and pitch angle-dependent magnetic drifts of substorm-injected ions. Further, it is primarily the leading edge of such injections, where the distribution is strongly ring-like, that the AC instability appears to be operating. By contrast, the ratio of the ring energy to the Alfvén energy remains well within the range of 0.25–4.0 suitable for IB instability throughout essentially all of the events, except those that occur in denser cold plasma of the outer plasmasphere.

Plain Language Summary One year's worth of plasma observations from geosynchronous orbit is examined for ion distributions that may simultaneously be subject to the ion Bernstein (IB) instability (generating fast magnetosonic waves) and the Alfvén cyclotron (AC) instability (generating electromagnetic ion cyclotron waves). Confirming past analyses, ring/shell distributions are commonly found primarily on the dayside of the magnetosphere. A new approach to high-fidelity representation of the observed ring/shell distribution functions allows statistical analysis of the ring/shell properties. Clear evidence is found for the operation of the AC instability, but only in the afternoon events, which are primarily produced by the energy- and pitch angle-dependent magnetic drifts of substorm-injected ions. Further, it is primarily at the leading edge of such injections, where the distribution is strongly ring-like, that the AC instability appears to be operating. By contrast, the IB instability seems to be driven throughout essentially all of the events, except those that occur in denser cold plasma of the outer plasmasphere. These results suggest that fast magnetosonic waves should typically dominate over electromagnetic ion cyclotron waves during most substorm injections.

1. Introduction

Among the many different types of waves observed within the Earth's magnetosphere, there is a class of fluctuations commonly observed near the magnetic equator, with frequency between the proton cyclotron frequency and the lower hybrid resonance frequency, known as fast magnetosonic waves (e.g., Gurnett, 1976; Kasahara et al., 1994; Laakso et al., 1990; Ma et al., 2013; Russell et al., 1970). Also known as ion Bernstein waves (Gary et al., 2010), they are now understood to be driven by proton velocity distributions with $\partial f_p(v_\perp)/\partial v_\perp > 0$ near $v_{||} = 0$, i.e., with a ring or shell-like shape (e.g., Chen et al., 2010, 2011; Gary et al., 2011; Ma et al., 2014; McClements et al., 1994; Perraut et al., 1982). Further, analysis shows that there is very little wave growth if the value of $v_\perp$ at which the slope of the phase space density is positive does not lie within a factor of ~2 of the local Alfvén speed, v_A (Chen et al., 2010). Fast magnetosonic waves have received particular attention in recent years because they may contribute to the acceleration of radiation-belt electrons (e.g., Horne et al., 2007; Horne & Thorne, 1998; Horne et al., 2000).

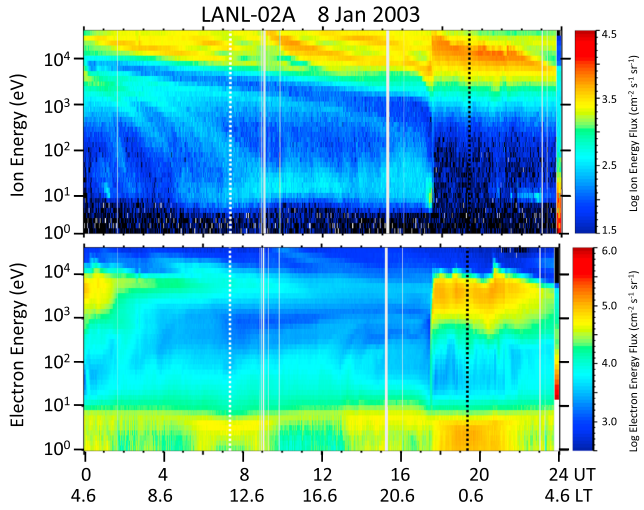

Figure 1. Color-coded ion and electron energy flux (proportional to count rate) observed by the MPA instrument on geosynchronous satellite LANL-02a on 8 January 2003. (top) Two features with $\partial f_p(v_\perp)/\partial v_\perp > 0$ near $v_{||} = 0$. The first corresponds to the ion population above the dark lane that progressively descends from ~5 keV at 0 UT to ~3 keV by ~10 UT, which is probably attributable to enhanced losses of ions drifting from the nightside close to the dense near-Earth exosphere and then out onto the dayside. The second is the energy-dispersed enhancement that begins above 30 keV at ~09 UT and drops to a few keV by 14 UT. The latter population arises from the energy-dependent drift of ions injected on the nightside during a substorm at ~0810 UT. The vertical dashed white and black lines mark local noon and midnight, respectively.

Ring or shell-like velocity distributions that may drive the ion Bernstein instability form from the energy-dependent drifts and losses experienced by plasma sheet/ring current ions as they move through the inner magnetosphere (e.g., Chen et al., 2010, 2011). As noted by previous authors, there are two plausible mechanisms for forming such velocity distributions: The first arises from discrete nightside injections of plasma sheet ions during substorms; because the ions with higher energies have larger gradient- and curvature-drift speeds, higher-energy particles outrun their lower energy counterparts as they drift around the inner magnetosphere, leading to an energy-dispersed enhancement in the dusk/afternoon sector. The second mechanism likewise involves energy-dependent drifts, which cause newly arriving plasma sheet ions to take energy-dependent paths through the inner magnetosphere; for a certain energy range, the drift trajectories penetrate deep into the inner magnetosphere, forming so-called "nose structures" in the ion distribution (e.g., see recent work by Ferradas et al., 2016, and references therein). Moreover, ions passing near the Earth encounter a region where the neutral exospheric density is higher, and thus, the losses to charge exchange are greatly enhanced. Particles emerging on such drift paths onto the dayside show significantly depleted fluxes compared to particles at other energies that have more successfully skirted the charge-exchange region. The resulting "deep ion minimum" is commonly observed in the dayside ion distribution function and features a clear positive gradient in phase space density above the minimum (e.g., Buzulukova et al., 2002; Kistler et al., 1989; Kovrazhkin et al., 1999).

These two ring/shell formation mechanisms tend to be manifested in different local time sectors: Energy-dispersed ion injections are typically seen in the afternoon/evening range of local time since ions injected in the midnight region drift generally westward and sunward in the combined magnetospheric electric and magnetic field. By contrast, the deep ion minimum appears in the prenoon sector (e.g., Kistler et al., 1989), where drift orbits that have passed through the dense near-Earth exosphere emerge onto the dayside. Near local noon evidence for both mechanisms can be found. Figure 1 shows an example of how both of these mechanisms are manifested at geosynchronous orbit. The figure shows ion and electron energy fluxes from the Los Alamos National Laboratory Magnetospheric Plasma Analyzer (LANL MPA) instrument on geosynchronous spacecraft LANL-02A (see section 2 for details of the MPA data set) plotted as a function of energy and time for the day 8 January 2003. The hot population of ions above ~1 keV in Figure 1a is the ion plasma sheet as it appears at geosynchronous orbit (L = 6.6). The energy-dispersed ion feature beginning above 30 keV at ~09 UT (13.6 LT) is the typical signature of substorm-injected ions in the afternoon sector. This event followed an isolated substorm that occurred at ~0810 UT (based on AE(12) provisional values provided by World Data Center for Geomagnetism, Kyoto *AE* index service). The dispersed ion injection was accompanied by a very weak, dispersed electron injection beginning at ~10 UT (Figure 1b). The difference in arrival time is because the ions travel westward from the nightside injection region, whereas the electrons drift eastward around the dawnside of the Earth. A second such ion injection (or more probably a drift echo of the first one) began at ~12 UT. Finally, a dispersionless and simultaneous ion and electron injection was observed just before 1800 UT (22.6 LT) near the substorm injection location, confirmed by a fairly weak *AE* increase of $<$100 nT.

At the beginning of the day and persisting for at least 12 h, the ion spectrogram also exhibits a dark lane of low energy flux starting around 4–5 keV and progressively declining with local time. This dark lane, seen primarily in the prenoon sector, identifies ion drift orbits that have suffered substantial losses through charge exchange during the passage from the nightside to the dayside of the magnetosphere. From Figure 1 it is clear how both of these mechanisms could give rise to ring/shell distributions with positive slopes in the phase space density in the few-keV energy range.

At geosynchronous orbit, which will be the focus of the present study, positive slopes in the phase space density ($\partial f_p(v_\perp)/\partial v_\perp > 0$) are relatively common. For a 4 day interval examined by Chen et al. (2011), ~25% of the distributions showed positive slopes, and they appeared to be associated with substorm injections on the nightside. The occurrence of positive slopes depends on local time and on magnetospheric activity, as indicated by the *Kp* index (Thomsen et al., 2011). The occurrence maximizes in the prenoon to postdusk local times and at lower values of *Kp*. Van Allen Probe observations also show that there are more nose events during quieter magnetospheric conditions than at more active times (Ferradas et al., 2016). At low *Kp*, ~20–30% of geosynchronous ion distributions between noon and 18 LT have a logarithmic slope ($f_p{}^{-1}\cdot\partial f_p(v_\perp)/\partial v_\perp$) greater than +0.3 at 8 keV (Thomsen et al., 2011). At progressively higher energies, the local time extent of positive slopes moves progressively toward earlier LT.

Recently, Min and Liu (2016) and Min et al. (2016) have pointed out that in addition to the ion Bernstein instability, ring-type ion distributions can also give rise to the Alfvén cyclotron (AC) instability if they are sufficiently anisotropic ($T_\perp/T_{||} > 0$). The resulting electromagnetic ion cyclotron (EMIC) waves have different nonlinear consequences from the fast magnetosonic waves produced by the ion Bernstein instability, corresponding to the nature of the free energy that drives them: Fast magnetosonic waves primarily produce energy diffusion in the perpendicular direction near the region of positive slope, whereas EMIC waves produce diffusion in pitch angle, reducing the anisotropy but resulting in little energy diffusion (Min & Liu, 2016). Particle-in-cell simulations of ring distributions show that EMIC waves can dominate the saturation wave power even if the initial ion Bernstein growth rate exceeds the Alfvén cyclotron growth rate. What determines the ultimate development of the two instabilities is the degree of anisotropy of the distribution, i.e., whether it is very ring-like ($T_{\perp r} >> T_{||r}$) or more shell-like ($T_{\perp r} \sim T_{||r}$). For the distributions they examined, Min et al. (2016) found that the AC instability dominated the wave power if the temperature anisotropy $T_{\perp r}/T_{||r}$ is greater than about 3. Based on the fact that EMIC and magnetosonic waves have not generally been reported together, Min et al. (2016) concluded that the ring distributions associated with fast magnetosonic waves in the magnetosphere are probably more shell-like, i.e., with temperature anisotropies generally less than 3.

In this work, we return to the geosynchronous ion distributions studied by Chen et al. (2011) and Thomsen et al. (2011) to examine the ring versus shell nature of distributions found to have positive slopes in the perpendicular velocity direction and to look for evidence that such distributions might also be subject to the AC instability. In particular, we find evidence that the temperature anisotropies of the ring/shell ion distributions have a clear upper limit that is apparently related to the parallel beta of the ring, $\beta_{||r} = 8\pi n_r T_{||r}/B^2$, where n_r is the density of the ring distribution, $T_{||r}$ is its temperature in the direction parallel to the magnetic field, and B is the magnitude of the magnetic field. Such an anisotropy bound, linked to the parallel beta of the distribution, has been identified as the signature of the AC instability (e.g., Gary et al., 1994, 1997).

We first describe a technique by which observed suprathermal ion distributions may be characterized as a sum of discrete ring beam distributions as described by Min & Liu (2015). Such ring beam distributions are amenable to analytical moment calculation (density and temperature, see Appendix A), as well as to the linear dispersion solver developed by Min and Liu (2015). Using the calculated ring densities and temperature components, we explore the statistical dependence of various relevant parameters on geomagnetic activity and local time. We further perform a superposed epoch analysis for a set of such events that exhibit a persistent presence for up to several hours. Finally, we present a case study of one such persistent event.

2. Data Selection

Data used in this study are the same as employed in our earlier paper (Thomsen et al., 2011): ion measurements from the Los Alamos Magnetospheric Plasma Analyzer (MPA) flown on a series of geosynchronous satellites (Bame et al., 1993). MPA is an electrostatic analyzer that covers the energy/charge range of ~1 eV/e to ~45 keV/e in 40 logarithmically spaced energy channels. With six channel electron multipliers providing polar angular resolution ~23° and 24 energy sweeps per 10 s spacecraft spin, the instrument provides a full 3-D velocity space measurement of ions or electrons every spin. Telemetry constraints only allow one 3-D distribution for each species to be transmitted every 86 s, so this is the basic time resolution of the measurements. The Los Alamos satellites do not carry magnetometers, but we are able to determine the magnetic field direction by identifying the symmetry axis of the three-dimensional particle distributions (Thomsen et al., 1999).

As described in our earlier paper (Thomsen et al., 2011), MPA ion data are sorted into 40 × 19 energy/pitch angle bins based on the orientation of the magnetic field determined from the anisotropy of the ion distribution itself. This field direction is derived by diagonalization of the three-dimensional hot-proton (*hp*) temperature matrix for measurements above ~100 eV/e. The derived direction and the corresponding parallel and perpendicular temperatures, $T_{hp||}$ and $T_{hp\perp}$, are reported in the standard MPA production moments. Since determination of the field direction depends on a significant anisotropy to this distribution, for this study we only use data for which the derived anisotropy $T_{hp\perp}/T_{hp||}$ exceeds 1.1.

Following the same procedure used in Thomsen et al. (2011), we identify distributions with positive slopes $\partial f_p(v_\perp)/\partial v_\perp$ near $v_{||} = 0$. As in our earlier work, we focus on energies above 1 keV, and we use the logarithmic derivative of the distribution, defined as the spectral slope from one energy channel to the next:

$$S(E_i) \equiv \frac{\log[f(E_i, \alpha = 90°)/f(E_{i-1}, \alpha = 90°)]}{\log[E_i/E_{i-1}]} \tag{1}$$

where E_i and $\alpha = 90°$ correspond to the *i*th energy channel and the tenth pitch angle bin. We impose the same requirements as previously regarding the number of counts in the two adjacent energy bins, and we employ a 5-point triangular smoothing in time to help remove statistical noise. Finally, in order to focus on very robust identifications, we use a more stringent requirement on the magnitude of $S(E_i)$ than used previously: Where the earlier analysis required $S(E_i) > 0.3$, we now set the threshold at $S(E_i) > 0.7$.

To obtain very high statistics, the earlier study employed nearly the entire multisatellite MPA data set, resulting in ~60 satellite years of data. For the present study, we use only one satellite year of data (spacecraft LANL-02A, for the year 2003), providing greater than 3.3×10^5 pitch angle distributions to examine, more than adequate to establish the properties we are interested in here.

3. Characterization of Distributions

To explore the properties of the ion Bernstein instability, previous authors have numerically integrated the full measured distribution, which allows examination of only a very limited number of samples (e.g., Chen et al., 2010, 2011; Ma et al., 2014) or have characterized ring beams as loss cone distributions (e.g., Horne et al., 2000) or subtracted Maxwellians (e.g., Denton et al., 2010; Gary et al., 2010; Liu et al., 2011; Xiao et al., 2013). In our experience, however, the actual observed ion distributions that satisfy the above $\partial f_p(v_\perp)/\partial v_\perp > 0$ condition are not well described by simple sums of bi-Maxwellians or subtracted Maxwellians. We have found it particularly difficult to accurately represent the pitch angle dependence of the distributions, especially for more shell-like shapes (see also discussion by Min & Liu, 2015).

We have therefore sought robust ways to characterize the observed MPA ring/shell distributions with high fidelity to the data but still with a form suitable for linear dispersion solver codes. With an eye to exploiting large satellite databases (e.g., MPA or data available from the Van Allen Probes mission), we have also sought a characterization that is not dependent on careful by-hand adjustments of the parameters.

The new approach we propose is motivated by the development of a dispersion solver that is based on ring beam velocity distributions (Min & Liu, 2015; Umeda et al., 2012), rather than the more conventional multiple bi-Maxwellian distributions. The dispersion solver of Min and Liu treats particle distributions as a sum of multiple individual ring beam distributions of the form (Umeda et al., 2012)

$$f_j(v_\perp, v_\parallel) = \frac{n_j}{\pi^{3/2}\theta_{\parallel j}\theta_{\perp j}^2\ C_j} e^{-\left(v_\parallel - v_{dj}\right)^2/\theta_{\parallel j}^2} e^{-\left(v_\perp - v_{rj}\right)^2/\theta_{\perp j}^2} \tag{2}$$

where *j* denotes the individual ring beam, v_{dj} is the parallel drift speed of the *j*th beam, v_{rj} is the radius of the velocity space ring, $\theta_{||j}$ and $\theta_{\perp j}$ characterize the thermal spread of the ring in the directions parallel and perpendicular to the magnetic field, and C_j is a constant of the form

$$C_j = e^{-v_{rj}^2/\theta_{\perp j}^2} + \sqrt{\pi}\left(\frac{v_{rj}}{\theta_{\perp j}}\right)\left[1 + \mathrm{erf}\left(\frac{v_{rj}}{\theta_{\perp j}}\right)\right] \tag{3}$$

For application to the observed ion distribution, we treat each measurement point (E_i,α_k) as a separate ring beam with density determined by the observed phase space density at that measurement point. The parallel drift speed and ring speed of each of these ring beams would be

$$v_{dj} = \sqrt{\frac{2E_i}{m_p}}\cos\alpha_k \tag{4a}$$

$$v_{rj} = \sqrt{\frac{2E_i}{m_p}}\sin\alpha_k \tag{4b}$$

where we assume that all ions are protons, with mass m_p.

In order to convert from a collection of discrete ring beams to a reasonably smooth distribution, we impose a finite ring thermal speed that is a fraction η of the velocity spacing between adjacent measurement points (see also Min & Liu, 2015). Specifically, we take

$$\begin{aligned}\theta_{\|}(i,k) = \theta_{\perp}(i,k) &= \eta\Delta v_{rms}(E_i,\alpha_k)\\ &= \frac{\eta}{2}sqrt\left[\left(\mathbf{v}_{ik}-\mathbf{v}_{i+1,k}\right)^2+\left(\mathbf{v}_{ik}-\mathbf{v}_{i-1,k}\right)^2+\left(\mathbf{v}_{ik}-\mathbf{v}_{i,k+1}\right)^2+\left(\mathbf{v}_{ik}-\mathbf{v}_{i,k-1}\right)^2\right]\end{aligned} \tag{5}$$

where $\mathbf{v}_{ik}$ is the vector velocity associated with the measurement point (E_i,α_k). Empirically, we find that for values of η less than about 0.25, the synthetic distribution produced by summing all the "observed" ring beams is granular, with significant gaps between the measurement points; on the other hand, if η is greater than about 0.5, the distribution is much smoother, but the overlap of adjacent ring beams produces an overestimate of the measured phase space density. As a reasonable compromise between smoothness and fidelity to the individual measurement points, we adopt a value of $\eta = 0.45$. We find that this choice of η has little effect on the temperatures derived for the ring/shell distributions we discuss below (see Appendix A), but it can result in slight (~few tens of percent) overestimate in the total ring/shell density.

The MPA observations consist of 40 energy channels (i) by 19 pitch angle channels (k), yielding 760 individual ring beams if the full observed distribution is used. To make the problem more tractable, we focus on the ring/shell itself by identifying all the measurement points that "belong to" each ring/shell according to the following procedure:

1. Identify the lowest energy $E_b = E_i$ where $S(E_i)$ in the perpendicular direction exceeds the threshold value of 0.7 (cf., equation (1)).
2. Take the value of $f(E_{b+1})$ at the energy level just below E_b to be the "floor" value, $f_{\min}$ (for MPA the energy channel numbers increase with decreasing energy).
3. Starting at energy level $i = b + 1$, step up in energy at $\alpha = 90°$, identifying all contiguous values of i where $f(E_i) > f_{\min}$.
4. At each value of i for which $f(E_i,\alpha = 90°) > f_{\min}$, search up and down in pitch angle, identifying all contiguous pitch angles for which $f(E_i,\alpha_k) > f_{\min}$.
5. The set of all measurement points (E_i,α_κ) where $f(E_i,\alpha_\kappa) > f_{\min}$ are attributed to the ring/shell. Note that only contiguous points with $f > f_{\min}$ are included. If f falls below $f_{\min}$ in either an $E_\perp$ or α search, that search is terminated.
6. For each MPA distribution where we find $S(E_b) > 0.7$, we compile the following quantities (see Appendix A for the details of the moment calculation):
   a. n_r = total density of the sum of all the ring beam elements of the identified ring/shell;
   b. $T_{\perp r}$ = perpendicular temperature of the sum of all the ring beam elements of the identified ring/shell;
   c. $T_{\|r}$ = parallel temperature of the sum of all the ring beam elements of the identified ring/shell;
   d. $V_{\|r}$ = parallel bulk flow speed of the sum of all the ring beam elements of the identified ring/shell; and
   e. $E_r = E_b$ = energy at which $S(E_b)$ first exceeds 0.7.

E_r is thus a measure of the ring/shell speed but is slightly lower than the peak f of the distribution.

Supplementing these ring/shell parameters, we also compile the relevant values from the production moment calculation, namely, n_{lp}, n_{hp}, $T_{\perp hp}$, and $T_{\|hp}$, where "lp" and "hp" correspond to the low-energy (<100 eV) and high-energy (>100 eV) ion populations analyzed in the production calculation of moments

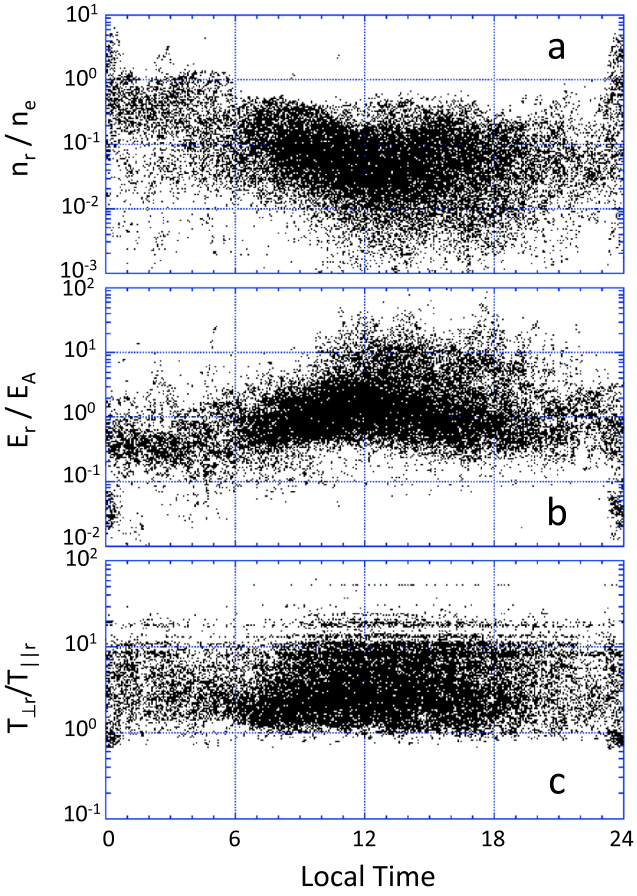

Figure 2. Local time dependence of properties computed for 32,577 individual 10 s ion distributions that exhibited a robust positive slope in the phase space density in the direction perpendicular to the magnetic field: (a) total ring/shell density, normalized to the total plasma density; (b) ring/shell energy (at which the positive slope occurs), normalized to the estimated Alfvén energy; and (c) perpendicular-to-parallel temperature ratio of the ring/shell distribution.

(cf., Thomsen et al., 1999). The total density of the plasma is taken to be the sum of the low- and high-energy populations, i.e., $n_{tot} = n_{lp} + n_{hp}$. Assuming charge neutrality, we take the total electron density to be $n_e = n_{tot}$.

In addition to the plasma and ring/shell parameters, we need to estimate the local magnetic field strength. As noted above, the spacecraft carrying MPA instruments do not carry magnetometers. Therefore, for the present purposes we simply approximate the field as a dipole, taking the local field strength at geosynchronous orbit to have a constant value of $B = 1.22 \times 10^{-3}$ G. We have explored the effect of using a local time-dependent field strength such as used by Gary et al. (1994), but we find that it makes very little difference to the results described below. The largest differences of course occur on the nightside, where the value of B is typically below the assumed dipole value, but as found in our earlier study (Thomsen et al., 2011), ion distributions with positive phase space density slopes above our threshold are dominantly seen on the dayside, so the effect of the common nightside field depression is not strongly reflected in our results. With this approximation to the magnetic field strength, we can then estimate the local Alfvén speed, $v_A = sqrt(B^2/4\pi n_e m_p)$; the corresponding Alfvén energy, $E_A = 0.5 m_p v_A^2$; and the ring/shell parallel beta, $\beta_{||r} = 8\pi n_r T_{||r}/B^2$.

Of the 3.3×10^5 pitch angle distributions available from LANL-02A measurements during 2003, we find 41,374 spectra with $S(E_b) > 0.7$. Of these, the requirement of a robust anisotropy ($T_{\perp hp}/T_{||hp} > 1.1$), as discussed above, reduces the available data to 32,577 individual 10 s distributions, approximately 10% of all the measurements in the year.

4. Results

To compare with our earlier results (Thomsen et al., 2011), we examined the local time, *Kp*, and energy dependence of the occurrence of ring/shell distributions (not shown here). Because of the significantly smaller amount of data and because of the imposition of a higher slope threshold, the statistics for the present data set are of course worse than those in the earlier study, but these data do reproduce the occurrence dependences found before, namely, that the occurrence rate of ring/shell distributions maximizes in the prenoon to postdusk sector, covering a broader LT range at lower *Kp*, and extending to earlier local times at higher energies.

Figure 2 summarizes the local time dependence of some of the derived beam properties: (a) the density of the ring/shell distribution relative to the total electron density (as estimated above), (b) the ring/shell energy relative to the local Alfvén energy, and (c) the ring/shell temperature anisotropy, $T_{\perp r}/T_{||r}$. The events with low E_r/E_A and large n_r/n_e near midnight turn out to be due to negative spacecraft charging events in which low-energy ambient ions are accelerated through the potential drop and arrive at the spacecraft with peak counts at energies above 1 keV. Our search for positive slopes in the distribution therefore falsely identifies such conditions as ring/shell distributions. We avoid these spurious events by restricting further attention to local times between 1 and 23 LT, where the great majority of the true ring/shell distributions are found. The existence of a few points in Figure 2a that are larger than 1 is due to the fact that, as mentioned above, the choice of a value η that is large enough to smooth out the lumpiness of the multiple-ring approximation to the observed distribution can also result in few tens of percent overestimate in the total ring/shell density.

Statistical analysis of the remaining events shows that the 5–95 percentile range for E_r/E_A is 0.26–8.4, corresponding to a range of v_r/v_A of 0.23 to 2.8. As mentioned above, significant growth of the ion Bernstein instability generally only occurs within the approximate range $0.5 < v_r/v_A < 2$ (Chen et al., 2010). Thus, a

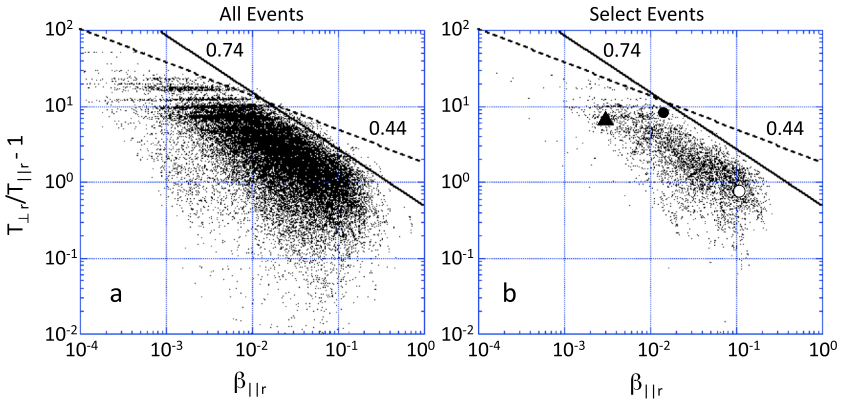

Figure 3. (a) Observed temperature anisotropy of each ring/shell distribution, plotted as a function of the estimated parallel beta of the distribution. There is a clear upper cutoff to the points in this representation that is roughly a power law in $\beta_{||r}$, with an exponent ~0.74 and a multiplicative constant of 0.451. (b) Same plot for a select set of clean, persistent ring/shell distributions. The black circle, white circle, and black triangle correspond to the individual pitch angle distributions illustrated in Figures 8b–8d, respectively.

large fraction of the ring/shell distributions we identify are suitably within the range for driving the instability. Similarly, the 5–95 percentile range of $T_{\perp r}/T_{||r}$ (Figure 2c) is 1.24–11.1, which is a suitable anisotropy to drive the Alfvén cyclotron instability. Thus, many of the distributions we have identified would appear to be within the parameter region where both instabilities may be playing a role in the evolution of the distribution, as suggested by Min and Liu (2016) and Min et al. (2016).

Figure 3a explores the relationship between the ring/shell temperature anisotropy and the parallel beta of the ring/shell distribution, which has been shown previously to provide a key signature of the operation of the Alfvén cyclotron instability (e.g., Gary et al., 1994, 1997; Gary & Lee, 1994). As shown by linear theory, hybrid numerical simulations, and magnetospheric observations in those and other papers, wave-particle scattering in the fluctuating fields of the instability leads to an upper limit of the temperature anisotropy of the form

$$\frac{T_{\perp p}}{T_{\|p}} - 1 = \frac{C_p}{\beta_{\|p}^{\alpha_p}} \tag{6}$$

where C_p and α_p are empirically determined constants. Such a limit may be taken as diagnostic of the operation of the Alfvén cyclotron instability, and it is clear from Figure 3a that the distributions in our ring/shell data set do indeed exhibit just such an upper limit. For these data, the exponent for the $\beta_{||r}$ dependence is ~0.74,

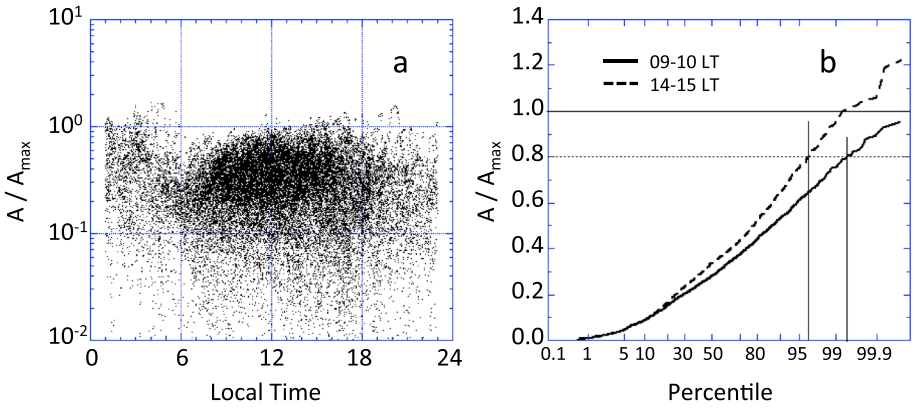

Figure 4. (a) Local time dependence of the anisotropy ($T_{\perp r}/T_{||r} - 1$), normalized to the limiting value $A_{max} = 0.451/\beta_{||r}^{0.74}$. (b) Occurrence probability distribution of the normalized anisotropy for two different local time sectors (9–10 LT and 14–15 LT). The afternoon sector tends to have more events with anisotropies approaching the limiting value A_{max}.

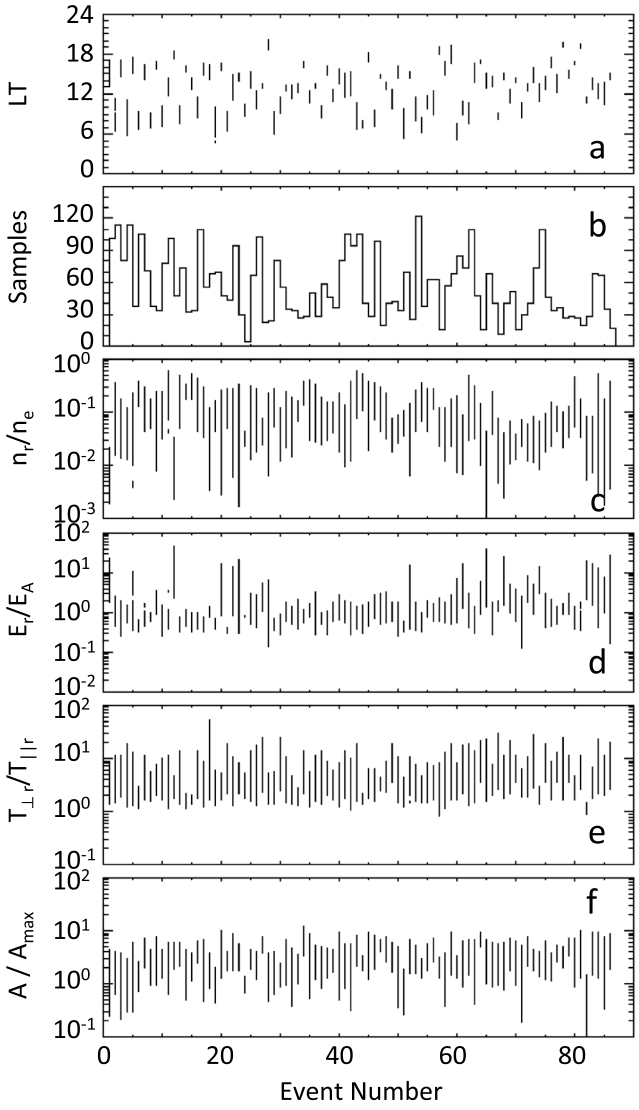

Figure 5. Selected properties of 86 ring/shell events identified by eye as having persistent and coherent determinations of the ring energy E_r. (a) Local time range of each event; (b) number of individual spectra (10 s spectrum every 86 s) in each event; (c) ring/shell density, normalized to the total plasma density; (d) ring energy, normalized to the Alfvén energy; (e) ring/shell temperature ratio; and (f) temperature anisotropy, normalized to the upper limit value determined from the full data set, $A_{max} = 0.451/\beta_{\|r}^{0.74}$.

with a possible tendency toward smaller values at lower values of $\beta_{\|r}$ (the solid and dashed lines in the figure illustrate exponents of 0.74 and 0.44). In both hybrid numerical simulations and Active Magnetospheric Particle Tracer Explorers/CCE magnetosheath observations, Gary et al. (1997) found the exponent α_p in equation (6) to be in the range of ~0.4–0.5, with higher values (~0.7–0.8) at larger $\beta_{\|p}$ (above ~2). While the exponent suggested by Figure 3a (~0.74) is larger than earlier work found in this range of $\beta_{\|}$, it is within the range of values found at higher $\beta_{\|}$ in both numerical simulations and spacecraft observations. Since previous work did not provide a physical explanation for the exact value of the exponent, we simply conclude that the very existence of the upper limit to the anisotropy shown in Figure 3a is strongly suggestive that the Alfvén cyclotron instability is at times driven by the ring/shell distributions we have identified, supporting the suggestion of Min and Liu (2016) and Min et al. (2016).

In equation (6), the constant C_p was found empirically from the simulations and observations in the magnetosheath to be ~1. We can estimate the corresponding constant for the data shown in Figure 3a by calculating the quantity

$$R = \beta_{\|r}^{0.74} \cdot (T_{\perp r}/T_{\|r} - 1) \tag{7}$$

and then identifying C_r as the value of R below which 99% of the measurement points lie. With this prescription we find that the anisotropy upper limit for the data in Figure 3a is expressed as

$$A_{max} = \left(\frac{T_{\perp r}}{T_{\|r}} - 1\right)_{max} = \frac{C_r}{\beta_{\|r}^{\alpha_r}} \tag{8}$$

with $(\alpha_r, C_r) = (0.74, 0.451)$. The curve labeled "0.74" in Figure 3a is a plot of $A_{max}(\beta_{\|r})$ with these parameters. For comparison, the curve labeled "0.44" is drawn for $(\alpha_r, C_r) = (0.44, 1.84)$. With $\alpha_r = 0.74$ and $C_r = 0.451$, we find that 82% of the points in Figure 3a have $A < 0.5A_{max}$, suggesting that the ring/shell anisotropy is not often strong enough to drive the AC instability; thus, it appears that the distributions we have identified are most frequently more shell-like than ring-like, in agreement with the conclusion of Min et al. (2016).

Figure 4a explores the local time dependence of the ring/shell anisotropy, relative to its maximum value (equation (8)). By construction, only 1% of the events have values of $A/A_{max} > 1$. Moreover, in the prenoon sector ($6 < LT < 12$), none of the anisotropy values seem to approach the maximum, suggesting that the ring/shell distributions seen in this region are not very ring-like. After noon there is a slightly larger fraction of events that push up against the upper limit, suggesting that it is here where the AC instability may at times be operating. This local time asymmetry is illustrated in Figure 4b, which compares the occurrence distributions of A/A_{max} from prenoon and postnoon intervals of 9–10 LT and 14–15 LT, respectively. While the difference is not large, it is clear that a larger fraction of the events approach the upper limit ($A/A_{max} = 1$) in the afternoon than in the prenoon sector. (The occurrence distributions simply plot the percentage of events that have A/A_{max} less than a given value, as a function of the value of A/A_{max}.)

The full set of events included in Figures 2–4 exhibit considerable scatter, and to make sure that the behavior we have described above is not an artifact of our automated selection process, we have obtained a very clean subset of the events by examining by eye the first 100 days of 2003 and identifying events with persistent and coherent determinations of the ring energy E_r. To avoid intervals of spacecraft charging, we have

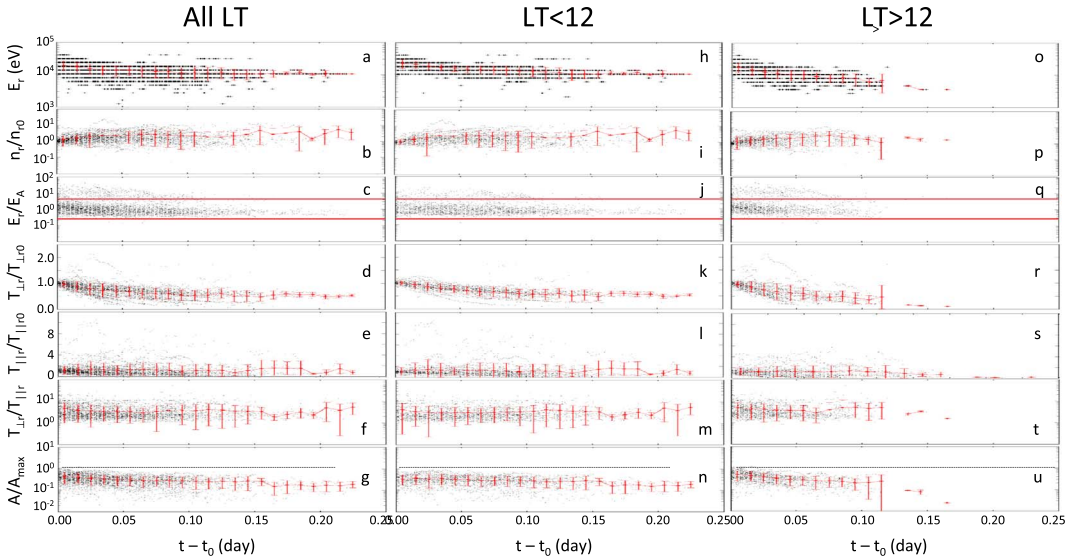

Figure 6. (a–u) Superposed-epoch analysis of various parameters measured during the 86 specially selected ring/shell intervals presented in Figure 5. The zero-epoch time is the time of the first spectrum in each interval that satisfies the ring/shell positive slope criterion. The left column contains all the events, while the middle column contains those that begin prior to noon local time, and the right column contains those that begin after noon local time. The red symbols indicate the means and standard deviations of the individual measurements in 0.01 day bins. The red lines in Figures 6c, 6j, and 6q bracket the range $0.25 < E_r/E_A < 4$, over which the ion Bernstein instability may potentially occur.

further restricted the selection to local times between 4 and 20 (earlier work with the MPA data set has shown that very few charging events are observed in this LT interval (Thomsen et al., 2013)).

Figure 5 presents compiled parameters for the 86 events identified by this manual process. The ranges of the parameters n_r/n_e, E_r/E_A, $T_{\perp r}/T_{||r}$, and $A/A_{\max}$ in this subset are quite representative of the full data set (cf., Figure 2). Figure 3b shows the distribution of anisotropy versus $\beta_{||r}$ of the select events for comparison with the full set shown in Figure 3a. The upper limit anisotropy found for the full data set also appears to apply to the select events.

As shown by Figure 5b, most of the specially selected events persisted for upwards of 30 samples (>45 min). They therefore provide the opportunity to examine the temporal evolution of the observed ring/shell distributions. Accordingly, for each of the 86 events, the time of the first identified ring/shell distribution has been found and denoted t_0. Figure 6 shows a superposed-epoch analysis of the 86 events, keyed to t_0 as the zero epoch. Figure 6 (left column) includes the full set of 86 events, while Figure 6 (middle and right columns)show just the events that begin before or after local noon, respectively. The prenoon and postnoon events are analyzed separately in order to see if there are any differences between ring/shell distributions most likely formed by losses during drift (primarily seen before noon, as mentioned above) and those most likely formed by energy-dependent drifts of newly injected ions (primarily seen postnoon).

The black symbols in each panel in Figure 6 show the individual measurements, and the red symbols show the mean values of the superposed parameters in 0.01 day bins in epoch time. The red error bars show the standard deviations in each of the bins. For these plots, the ring/shell density and perpendicular and parallel temperatures are all normalized to the values they had at t_0, denoted with the subscript "0."

The most prominent feature of the evolution of the ring/shell distributions is the tendency for the ring energy, E_r, to decrease with epoch time, both prenoon and postnoon (Figures 6a, 6h, and 6o). This decrease is consistent with both the energy-dependent drift dispersion expected for substorm-injected ions and with the time (or local time) dependence of the deep ion minimum in the dayside ion distributions associated with strong losses during drifts deep into the near-Earth region. Similarly, the tendency for the ring/shell density to increase during the first hour or so of the events (Figures 6b, 6i, and 6p) is consistent with the inclusion of more of the hot-ion population as the cutoff energy decreases.

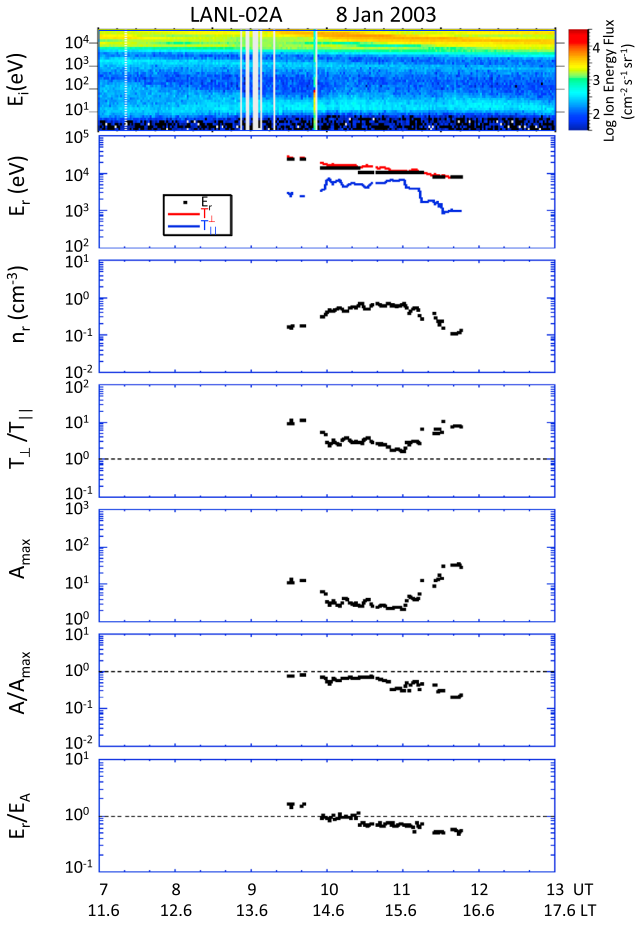

Figure 7. Case study of one of the 86 selected ring/shell events in Figure 5. (a) Energy-time spectrogram of ion energy-flux; (b) identified ring/shell energy (black squares) and ring/shell perpendicular (red) and parallel (blue) temperatures; (c) ring/shell density; (d) temperature ratio; (e) estimated upper limit anisotropy, $A_{max} = 0.451/\beta_{||r}^{0.74}$; (f) ring/shell anisotropy normalized to the limiting value; and (g) ring/shell energy normalized to the estimated Alfvén energy. This event, observed on 8 January 2003, is the energy-dispersed, substorm-injected ion distribution identified in Figure 1. The onset was at ~0930 UT, at a local time ~14 LT, and it persisted with declining E_r for ~2.5 h. E_r/E_A was within the ion Bernstein zone of 0.25–4 for the entire event, and for the first half of the event the normalized anisotropy approached 1, suggesting the operation of the Alfvén cyclotron instability as well.

The third set of panels (Figures 6c, 6j, and 6q) shows the ratio of the ring energy to the Alfvén energy, with the horizontal red lines demarcating the region between 0.25 and 4.0, the range within which significant fast magnetosonic wave growth is potentially possible (Chen et al., 2010). As seen in these panels, there appear to be two different populations in our data set: One that generally lies well within this range and another with values substantially above 4. We attribute the latter to ring/shell distributions that overlap the outer plasmasphere at geosynchronous orbit, where the Alfvén speed is reduced by the large cold plasma density, resulting in large ratios of E_r/E_A.

The behavior of the perpendicular temperature follows that of the ring energy, decreasing with time as lower energy particles arrive or as the energy of the deep ion minimum drops with local time (Figures 6d, 6k, and 6r). There is no clear trend in the parallel temperature (Figures 6e, 6l, and 6s), and there is a much broader scatter than in the perpendicular temperature (note the difference in scales in the two panels). There may be a slight tendency for the anisotropy to decrease initially, but it is far from clear in either the prenoon or postnoon events (Figures 6f, 6m, and 6t). On the other hand, the ratio of the anisotropy to the maximum value determined above, A/A_{max}, does clearly tend to drop further below 1 as epoch time increases (Figures 6g, 6n, and 6u), but comparison of Figures 6n and 6u shows that it is largely the postnoon events that show this tendency. The fact that the ring/shell anisotropy only pushed up near the maximum allowed value after local noon was noted above in Figure 4 for the full data set.

The decrease in A/A_{max} in the afternoon sector suggests that only the leading edge of an injection may be unstable to the Alfvén cyclotron instability, with the population arriving later having a more shell-like character. Moreover, the absence of such a tendency in the prenoon events suggests that the AC instability does not play much of a role in regulating the anisotropy of the plasma sheet ions that successfully drift out through the dayside magnetosphere at energies just above those where significant drift losses occur.

To illustrate the general behavior for likely substorm-injected ring/shell ions with a specific case study, Figure 7 presents the observations from one of the intervals identified in the manually selected events, from 8 January 2003 (see also Figure 1), when the spacecraft was moving from noon to dusk. The zero epoch time t_0 for this event was 0930 UT, when the spacecraft was at a local time of 14.1 LT. This is the first substorm injection event identified in Figure 1. Figure 7a shows the color-coded ion energy flux as a function of energy and time through the event. The injected ions that form the identified ring/shell distribution can be seen arriving around 0930 UT, and the energy of this population progressively declines over the course of the next 2 h. Figure 7b shows the identified ring/shell energy E_r and the computed perpendicular and parallel temperatures. As expected, the $T_{\perp r}$ follows E_r quite closely, and both decline with time. The computed ring/shell density increases initially (Figure 7c), then declines toward the end of the interval. The anisotropy (Figure 7d) is initially rather high, declines through the event, and then increases again near the end. Figure 7e shows the computed A_{max} (equation (8)), which tracks the inverse of the parallel temperature (Figure 7b). As seen in the superposed-epoch study, the ratio A/A_{max} is initially near 1 but gradually declines through the event. Finally, the ratio of the ring/shell energy to the estimated local Alfvén energy declines progressively through the event from slightly greater than 1 to somewhat less than 1, well within the range required for the ion Bernstein instability.

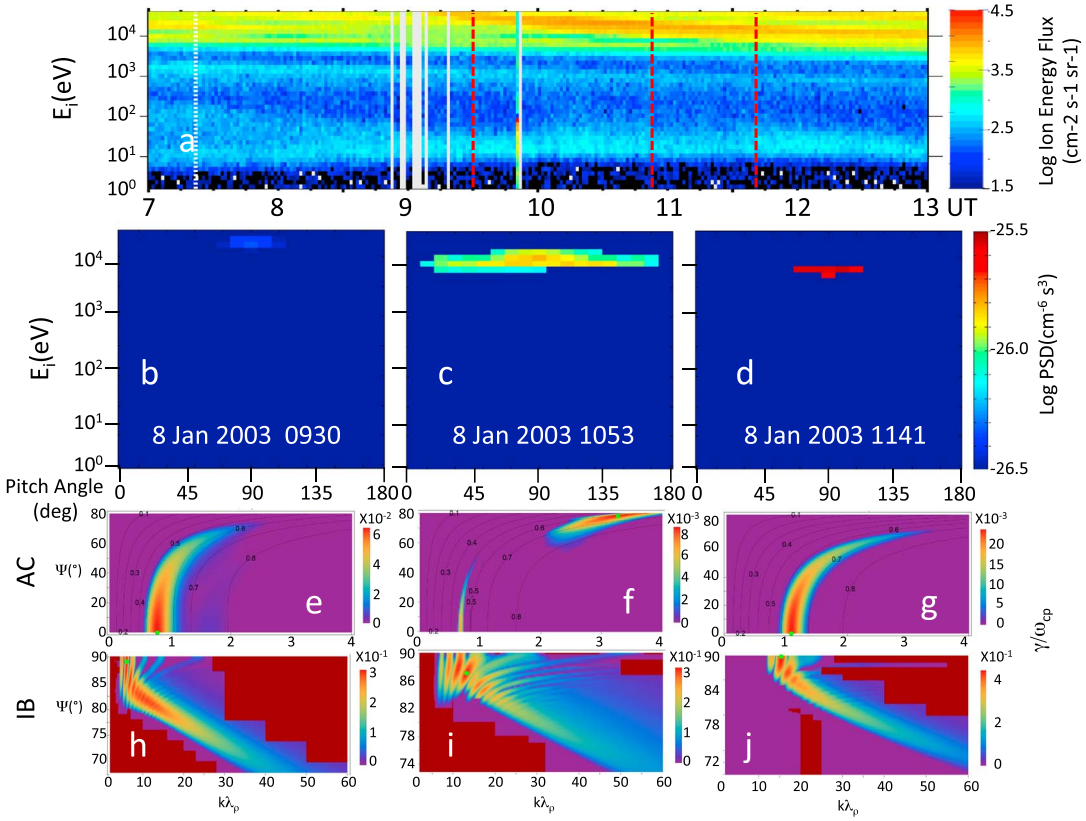

Figure 8. Energy/pitch angle distributions and calculated growth rates for three selected intervals within the ring/shell event of Figure 7. (a) Ion energy-time spectrogram with the times of the individual spectra marked; (b) ring-like individual spectrum observed at 0930 UT, early in the event; (c) shell-like spectrum observed at 1053 UT, in the middle of the event; and (d) more ring-like distribution observed at 1141 UT, near the end of the event. (e–g) Growth rate of the Alfvén cyclotron instability (normalized to the ion gyrofrequency) for the three spectra in Figures 8b–8d, plotted as a function of wave normal angle (ψ) and wave number ($k\lambda_p$), where $\lambda_p = c/\omega_{pp}$. (h–j) Growth rate of the ion Bernstein instability for the three spectra in Figures 8b–8d. The green dot in each growth rate panel marks the point of maximum growth rate.

Figure 8 shows the full energy/pitch angle distributions for three selected spectra during the interval in Figure 7 (for clarity, we display only the phase space density values corresponding to the identified ring/shell distribution). Figure 8a reproduces the ion energy-flux spectrogram from Figure 7a, with the red dashed vertical lines indicating the times at which the three spectra in the bottom row were observed. The distribution in Figure 8b, from near the zero epoch time of the event, is very ring-like, i.e., strongly confined to near 90° pitch angle, consistent with the large initial value of $T_{\perp r}/T_{||r}$ seen in Figure 7d. With A/A_{max} near 1 (Figure 7f and black filled circle in Figure 3b), it appears that the anisotropy of this distribution has been limited by action of the Alfvén cyclotron instability.

The distribution in Figure 8c was observed well after the onset of the event and shows a denser and very shell-like distribution, extending over nearly the full range of pitch angle. Correspondingly, $T_{\perp r}/T_{||r}$ approached 1 during this interval (Figure 7d). While the maximum allowed anisotropy was lower at this time (Figure 7e) because $T_{||r}$ had increased (Figure 7b), A/A_{max} had still dropped well below 1 (Figure 7f and white filled circle in Figure 3b). Thus, by 1053 UT, the distribution was probably no longer driving the Alfvén cyclotron instability.

The distribution in Figure 8d, observed near the end of the ring/shell event, again appears rather ring-like, being concentrated near 90 pitch angle, and had a correspondingly large $T_{\perp r}/T_{||r}$. One might thus suspect it to be AC-unstable; however, as seen in Figure 7e, A_{max} was larger compared to its earlier values (due to the low value of $T_{||r}$), so in fact A/A_{max} was well below 1 (Figure 7f and black triangle in Figure 3b), and the AC instability was unlikely to be in play.

5. Summary and Discussion

An analysis of 1 year of geosynchronous plasma observations, using the same identification scheme employed previously (Thomsen et al., 2011), but with a more stringent requirement on $\partial f_p(v_\perp)/\partial v_\perp$ near $v_{||} = 0$, confirms that ring/shell-like ion distributions that can potentially give rise to the ion Bernstein instability are quite common at geosynchronous orbit. The same LT-*Kp* dependence of the occurrence of such distributions is also found.

We have introduced a new approach to characterizing the full observed energy/pitch angle distribution, which involves treating each measurement point (E_i,α_k) as a separate ring beam of the form of equation (2). The observed distribution is then taken as the sum of the individual ring beams that are identified as "belonging" to the ion population with the positive $\partial f_p(v_\perp)/\partial v_\perp$. This approach not only enables a high-fidelity representation of the observations that can be analytically integrated to form moments of the ring/shell distribution but it also enables the stability of the distribution to be assessed with a linear dispersion solver developed by Min and Liu (2015).

MPA measurements provide only the energy-per-charge of incident ions, and all of the calculated moments of the ring/shell distributions, as well as the total density of the full distribution, assume that all the ions are protons. In reality, composition-capable measurements show that the heavy-ion contribution to magnetospheric fluxes varies appreciably with L, LT, and *Kp*, and heavy ions may dominate the fluxes above 10 keV under some circumstances (e.g., Fernandes et al., 2017; Ferradas et al., 2016). However, at geosynchronous orbit, at the relatively low values of *Kp* that favor the production of ring/shell distributions (e.g., Thomsen et al., 2011), protons are typically the dominant species at the energies of interest (e.g., Fernandes et al., 2017). It would be of interest to repeat elements of this study with composition data and actual magnetic field measurements (e.g., with data from the Van Allen Probes), to see what quantitative effect the actual composition has.

With the moments of the identified ring/shell distributions computed as described in the Appendix A, and with the magnetic field approximated as a dipole, other properties of the identified ring/shell distributions can be analyzed statistically. In particular, for a large fraction of the ring/shell distributions identified here, the ratio of the ring/shell speed to the local Alfvén speed is within the range of 0.5–2 that has previously been determined as conducive to the ion Bernstein instability (Chen et al., 2010).

Further, temperature anisotropies of these ring/shell distributions have been examined to explore whether or not such distributions might also drive the Alfvén cyclotron instability as well as the IB instability, as suggested by Min and Liu (2016) and Min et al. (2016). When plotted as a function of the parallel beta of the ring/shell, $\beta_{||r}$, the temperature anisotropy ($T_{\perp r}/T_{||r} - 1$) is found to have a clear upper limit of the form

$$A_{\max} = \left(\frac{T_{\perp r}}{T_{||r}} - 1\right)_{\max} = \frac{0.451}{\beta_{||r}^{0.74}} \tag{9}$$

In previous work, such a β-dependent upper limit to the anisotropy has been found to be diagnostic of the operation of the Alfvén cyclotron instability (e.g., Gary et al., 1994). Thus, it appears that the AC instability does play a role in modulating the anisotropy of the ring/shell distributions at geosynchronous orbit. Earlier work based on theoretical arguments, numerical simulations, and satellite data suggested that the exponent of $\beta_{||}$ in equation (9) is more typically of the order 0.4–0.5 in the range of $\beta_{||}$ covered here; however, those studies did find exponents trending to higher values (~0.7–0.8) at higher values of $\beta_{||}$, and at this point it is not clear what physically determines this exponent. We leave this as a question for future study.

While clear evidence has been presented that the AC instability is probably limiting the temperature anisotropy of ring/shell distributions at geosynchronous orbit, most of the measured anisotropies are well below the upper limit (Figure 4). Thus, it appears that the AC instability is not very often driven by the ring/shell distributions, suggesting that they are typically more shell-like than ring-like. However, we also find that $A/A_{\max}$ can be well below 1 even for very ring-like distributions ($T_{\perp r} >> T_{||r}$) because $A_{\max}$ depends inversely on $T_{||r}$ (equation (9)).

Events with $A/A_{\max}$ near 1, which suggest the action of the AC instability, are generally found only after local noon, where ring/shell distributions are most likely produced by energy-dispersed ions injected on the night side during substorms. In the prenoon region, where ring/shell distributions are most likely produced by the

deep ion minimum attributable to strong charge-exchange losses during ion drift through the dense near-Earth exosphere, there is little evidence that the AC instability is playing a role in limiting the anisotropy of the drifting ions. Thus, the AC instability appears to be primarily a consequence of dispersive drifts of substorm-injected ions. It should be emphasized, however, that this conclusion applies only to distributions first identified as ring/shell type. We have not examined the more general occurrence probability of AC-unstable distributions that do not satisfy the ring/shell requirement of $(\partial f_p(v_\perp)/\partial v_\perp > 0)$. An analysis of the occurrence of EMIC waves themselves (Saikin et al., 2016) reveals a fairly strong dayside preference, with prenoon occurrence dominating during times of low *AE* and a stronger afternoon occurrence during disturbed times of high *AE*. It seems probable that the multiple injections that occur during disturbed times would tend to overlap in the afternoon sector, reducing the probability of finding IB-unstable distributions but not reducing the activity of the AC instability. This would explain the finding here and previously that IB-unstable distributions exist primarily during quieter intervals.

The prenoon/postnoon difference in A/A_{max} is also observed in superposed-epoch analyses of a subset of 86 ring/shell distributions that have been selected for persistent and coherent identified values of the ring energy. With the zero epoch for each persistent event taken to be the observation time of the first distribution that met the positive-slope condition, a clear decline in A/A_{max} from values near 1 to values well below 1 is seen, but only postnoon. In addition to this local time-dependent behavior of A/A_{max}, the most prominent variations with epoch time are a decline of the ring energy E_r, a decline of the perpendicular ring temperature $T_{\perp r}$ (which is of course related to E_r), and a slight increase in the ring density n_r. None of these latter three variations appear to depend on the local time sector and indeed are expected for both formation mechanisms of ring/shell distributions.

A case study of one persistent postnoon event illustrates the behavior suggested by the superposed-epoch analysis. The event is an energy-dispersed ion injection from an earlier substorm on the nightside of the magnetosphere. As also seen in the superposed-epoch analysis of postnoon events, this event began with a strong temperature anisotropy, perhaps due to the pitch angle dependence of gradient and curvature drifts of the injected particles: The azimuthal drift speed of such particles consists of an electric field drift common to all particles, plus a magnetic drift that is proportional to $\sim(0.7 + 0.3\ \sin\alpha_{eq})E$, where E is the energy of the particle and α_{eq} its equatorial pitch angle (e.g., Hamlin et al., 1961). Early in the event the particles that arrive first are thus those with larger energies and pitch angles close to 90° (Figure 8b). Later, lower energy particles begin to arrive, along with particles with smaller pitch angles, and the ring/shell distribution evolves from a very ring-like shape to a much more shell-like shape (Figure 8c). It is not clear why the distribution returns to ring-like near the end of the event (Figure 8d), but by then A_{max} has evolved to larger values so that only the leading edge of the event exhibits A/A_{max} values near 1.

Figures 8e–8g show the color-coded Alfvén cyclotron growth rate (normalized to the proton gyrofrequency) for the same three spectra, calculated using the multi ring beam dispersion solver of Min and Liu (2015) with the observed distributions providing the ring beam properties, as described in section 3. Figures 8h–8j similarly show the calculated ion Bernstein growth rate. The maximum γ/ω_{cp} for the AC instability in Figures 8e–8g is (0.065, 0.0086, 0.024), confirming the qualitative inference based on A/A_{max}. It appears that the evolution of the pitch angle distribution results in the leading edge of drifting injections most strongly driving the AC instability.

Similarly, Figures 8h–8j show the calculated ion Bernstein growth rate for the three spectra. All three distributions show very strong calculated growth. The maximum values of γ/ω_{cp} for the IB instability in Figures 8h–8j are (0.31, 0.33, 0.45), consistent with the fact that throughout the entire event the ratio of the ring/shell energy to the Alfvén energy stayed well within the range 0.25–4 for operation of the IB instability (Chen et al., 2010). The very large calculated IB growth rates compared to the AC values suggest that at saturation the magnetosonic waves driven by these distributions may dominate the wave spectra. Therefore, while we confirm the original conjecture of Min and Liu (2016) and Min et al. (2016) that ring-like ion distributions in the magnetosphere may give rise to both EMIC and fast magnetosonic waves, significant contributions from the AC instability may largely be limited primarily to the leading edge of substorm-injected ion populations. This finding thus confirms the conclusion reached by Min et al. (2016).

The trend noted above for E_r/E_A to decline over the course of an event is clearly seen in this event (Figure 7g). A decline in E_r/E_A over the course of an event suggests a corresponding shift in the

unstable IB wave frequency from lower harmonics to higher harmonics (Chen et al., 2010). This shift can indeed be seen in Figures 8h–8j, which show a progressive increase in $k\lambda_p$ at peak growth (green dots) over the course of the event.

6. Conclusions

Observational evidence for the probable operation of both the ion Bernstein instability and the Alfvén cyclotron instability at geosynchronous orbit exists in the form of ring/shell-like ion distributions commonly found in both the prenoon and postnoon regions of the magnetosphere. A new approach to high-fidelity representation of the observed ring/shell distribution functions in a form readily suited to both analytical moment calculation and linear dispersion analysis has been presented.

The resulting data set of events with robust $\partial f_p(v_\perp)/\partial v_\perp > 0$ near $v_{||} = 0$ shows that the ring/shell anisotropy has a clear upper limit that depends on the parallel beta of the ring/shell ($\beta_{||r}$) in a manner that is diagnostic of the operation of the AC instability. This upper limit is only reached in the postnoon events, which are primarily produced by the energy- and pitch angle-dependent magnetic drifts of substorm-injected ions. Further, it is only in the leading edge of such injections, where the distribution is strongly ring-like, that the AC instability appears to be operating. By contrast, the ratio of the ring energy to the Alfvén energy remains well within the range 0.25–4.0 suitable for IB instability (Chen et al., 2010) throughout essentially all of the events, both prenoon and postnoon, except those that occur in denser cold plasma of the outer plasmasphere.

We therefore conclude that at geosynchronous orbit, ring/shell distributions that fall within the IB-unstable range $0.25 < E_r/E_A < 4.0$ are quite common. Such distributions are also subject to the AC instability, although that instability is probably primarily driven by the highly ring-like distributions at the leading edge of substorm-injected ions in the afternoon sector.

Appendix A: Ring Beam Moments

As described above, the data analysis procedure employed here treats an observed ion ring/shell distribution as the sum of a number of ring beams with individual phase space density functions specified as in equation (2), reproduced here for completeness:

$$f_j(v_\perp, v_\parallel) = \frac{n_j}{\pi^{3/2}\theta_{\parallel j}\theta_{\perp j}^2 C_j} e^{-\left(v_\parallel - v_{dj}\right)^2/\theta_{\parallel j}^2} e^{-\left(v_\perp - v_{rj}\right)^2/\theta_{\perp j}^2} \tag{A.1}$$

where

$$C_j = e^{-v_{rj}^2/\theta_{\perp j}^2} + \sqrt{\pi}\left(\frac{v_{rj}}{\theta_{\perp j}}\right)\left[1 + \text{erf}\left(\frac{v_{rj}}{\theta_{\perp j}}\right)\right] \tag{A.2}$$

The phase space density measured at each instrument measurement point specifies one such ring beam, each of which corresponds to a gyrotropic distribution moving with an average velocity v_{dj} parallel to the magnetic field direction. The parameters v_{dj}, v_{rj}, $\theta_{\perp j}$, and $\theta_{||j}$ are specified from the observations according to equations (4a) and (4b) and (5) above.

The total density of a ring/shell distribution composed of N such ring beam s is

$$n_r = \sum_{j=1}^{N} n_j \tag{A.3}$$

The average parallel velocity of the total ring/shell distribution is

$$V_{\parallel r} = \frac{1}{n_r}\sum_{j=1}^{N} n_j v_{dj} \tag{A.4}$$

For the ring/shell distributions identified in MPA data for this study, the average parallel velocity is generally consistent with zero, as expected for particles trapped within the geomagnetic field, but we nonetheless carry it throughout the following calculations.

The parallel and perpendicular temperatures of the full ring/shell distribution are (Min et al., 2016; equation (3); taking into account the net parallel flow velocity):

$$T_{\parallel} = \frac{m}{n_r}\int (v_{\parallel} - V_{\parallel})^2 \left[\sum_{j=1}^{N} f_j(v_{\perp}, v_{\parallel})\right] d^3v \tag{A.5}$$

$$T_{\perp} = \frac{m}{2n_r}\int {v_{\perp}}^2 \left[\sum_{j=1}^{N} f_j(v_{\perp}, v_{\parallel})\right] d^3v \tag{A.6}$$

where we have assumed only a single species, so $m_j = m$.

Interchanging the integration and summation, equations (A.5) and A.(6)) become

$$\begin{aligned} T_{\parallel} = \frac{2\pi m}{n_r}\sum_{j=1}^{N} A_j \Bigg[& \int_{-\infty}^{\infty} v_{\parallel}^2 e^{-\left(v_{\parallel}-v_{dj}\right)^2/\theta_{\parallel j}^2} dv_{\parallel} \int_{0}^{\infty} v_{\perp} e^{-\left(v_{\perp}-v_{rj}\right)^2/\theta_{\perp j}^2} dv_{\perp} \\ & -2V_{\parallel r} \int_{-\infty}^{\infty} v_{\parallel} e^{-\left(v_{\parallel}-v_{dj}\right)^2/\theta_{\parallel j}^2} dv_{\parallel} \int_{0}^{\infty} v_{\perp} e^{-\left(v_{\perp}-v_{rj}\right)^2/\theta_{\perp j}^2} dv_{\perp} \\ & + V_{\parallel r}^2 \int_{-\infty}^{\infty} e^{-\left(v_{\parallel}-v_{dj}\right)^2/\theta_{\parallel j}^2} dv_{\parallel} \int_{0}^{\infty} v_{\perp} e^{-\left(v_{\perp}-v_{rj}\right)^2/{\theta_{\perp j}}^2} dv_{\perp} \Bigg] \end{aligned} \tag{A.7}$$

$$T_{\perp} = \frac{2\pi m}{2n_r}\sum_{j=1}^{N} A_j \left[\int_{-\infty}^{\infty} e^{-\left(v_{\parallel}-v_{dj}\right)^2/\theta_{\parallel j}^2} dv_{\parallel} \int_{0}^{\infty} v_{\perp}^3 e^{-\left(v_{\perp}-v_{rj}\right)^2/\theta_{\perp j}^2} dv_{\perp}\right] \tag{A.8}$$

where.

$$A_j = \frac{n_j}{\pi^{3/2}\theta_{\parallel j}\theta_{\perp j}^2 C_j}.$$

We need the following five integrals:

$$I_1 = \int_{-\infty}^{\infty} x^2 e^{-(x-a)^2/b^2} dx = \frac{\sqrt{\pi}}{2}\left(b^3 + 2a^2 b\right)$$

$$I_2 = \int_{-\infty}^{\infty} x e^{-(x-a)^2/b^2} dx = ab\sqrt{\pi}$$

$$I_3 = \int_{-\infty}^{\infty} e^{-(x-a)^2/b^2} dx = b\sqrt{\pi}$$

$$\begin{aligned} I_4 &= \int_{0}^{\infty} x e^{-(x-a)^2/b^2} dx \\ &= \frac{ab\sqrt{\pi}}{2}\left[1 + \operatorname{erf}\left(\frac{a}{b}\right)\right] + \frac{b^2}{2} e^{-a^2/b^2} \end{aligned}$$

$$\begin{aligned} I_5 &= \int_{0}^{\infty} x^3 e^{-(x-a)^2/b^2} dx \\ &= \frac{ab\sqrt{\pi}}{4}\left(2a^2 + 3b^2\right)\left[1 + \operatorname{erf}\left(\frac{a}{b}\right)\right] + \frac{b^2}{2}\left(a^2 + b^2\right) e^{-a^2/b^2} \end{aligned}$$

With these integrals, equations (A.7) and A.(8) become

$$
\begin{aligned}
T_{\parallel} &= \frac{2\pi m}{n_r}\sum_{j=1}^{N}\frac{n_j}{\pi^{3/2}\theta_{\parallel j}\theta_{\perp j}^2 C_j}\left[\frac{\sqrt{\pi}}{2}\left(\theta_{\parallel j}^3+2v_{dj}^2\theta_{\parallel j}\right)-2V_{\parallel r}v_{dj}\theta_{\parallel j}\sqrt{\pi}+V^2{}_{\parallel r}\theta_{\parallel j}\sqrt{\pi}\right]\\
&\cdot\left\{\frac{v_{rj}\theta_{\perp j}\sqrt{\pi}}{2}\left[1+\operatorname{erf}\left(\frac{v_{rj}}{\theta_{\perp j}}\right)\right]+\frac{\theta_{\perp j}^2}{2}e^{-v_{rj}^2/\theta_{\perp j}^2}\right\}\\
&= \frac{2\pi m}{n_r}\sum_{j=1}^{N}\frac{n_j}{\pi^{3/2}\theta_{\parallel j}\theta_{\perp j}^2 C_j}\\
&\cdot\left[\frac{\sqrt{\pi}}{2}\left(\theta_{\parallel j}^3+2v_{dj}^2\theta_{\parallel j}\right)-2V_{\parallel r}v_{dj}\theta_{\parallel j}\sqrt{\pi}+V_{\parallel r}^2\theta_{\parallel j}\sqrt{\pi}\right]\cdot\frac{\theta_{\perp j}^2}{2}C_j\\
&= \frac{m}{n_r}\sum_{j=1}^{N}n_j\left[\frac{\theta_{\parallel j}^2}{2}+\left(v_{dj}-V_{\parallel r}\right)^2\right]
\end{aligned}
\tag{A.9}
$$

and

$$
\begin{aligned}
T_{\perp} &= \frac{\pi m}{n_r}\sum_{j=1}^{N}\frac{n_{rj}}{\pi^{3/2}\theta_{\parallel j}\theta_{\perp j}^2 C_j}\left(\theta_{\parallel j}\sqrt{\pi}\right)\left(\frac{\theta_{\perp j}^2}{2}\right)\\
&\cdot\left\{\frac{\sqrt{\pi}}{2}\frac{v_{rj}}{\theta_{\perp j}}\left(2v_{rj}^2+\theta_{\perp j}^2\right)\left[1+\operatorname{erf}\left(\frac{v_{rj}}{\theta_{\perp j}}\right)\right]+\left(v_{rj}^2+\theta_{\perp j}^2\right)e^{-v_{rj}^2/\theta_{\perp j}^2}\right\}\\
&= \frac{m}{n_r}\sum_{j=1}^{N}\frac{n_j}{2C_j}\left\{v_{rj}^2C_j+\frac{3}{2}\theta_{\perp j}^2\left[C_j-\frac{1}{3}e^{-v_{rj}^2/\theta_{\perp j}^2}\right]\right\}\\
&= \frac{m}{n_r}\sum_{j=1}^{N}\frac{n_j}{2}\left\{v_{rj}^2+\frac{3}{2}\theta_{\perp j}^2\left[1-\frac{1}{3C_j}e^{-v_{rj}^2/\theta_{\perp j}^2}\right]\right\}
\end{aligned}
\tag{A.10}
$$

To validate these expressions, we have used them to calculate the anisotropies of all of the two-component proton distributions presented in Table 1 of Min et al. (2016). We have applied equations (A.9) and (A.10) to the sets of 12 ring beams that approximate each of the partial shell distributions (cf., equations (1) and (4a) and (4b)) (Min et al., 2016) listed in that table. The resulting computed anisotropies $T_{\perp}/T_{\parallel}$ agree exactly with the anisotropy values listed in the table, which were calculated from the partial shell distributions in that study (equation (1)) (Min et al., 2016).

Acknowledgments
Work at PSI was supported by NSF collaborative research grant 1303675. M.F.T. gratefully acknowledges support as a Guest Scientist at Los Alamos National Laboratory. Work of S.P.G., K.L., and K.M. was supported by NASA grant NNX16AM98G. The MPA data used in this study are available upon request from the first author.

References

Bame, S. J., McComas, D. J., Thomsen, M. F., Barraclough, B. L., Elphic, R. C., Glore, J. P., … Wymer, F. J. (1993). Magnetospheric plasma analyzer for spacecraft with constrained resources. *The Review of Scientific Instruments*, *64*(4), 1026–1033. https://doi.org/10.1063/1.1144173

Buzulukova, N. Y., Galperin, Y. I., Kovrazhkin, R. A., Glazunov, A. L., Vladimirova, G. A., Stenuit, H., … Delcourt, D. C. (2002). Two types of ion spectral gaps in the quiet inner magnetosphere: Interball-2 observations and modeling. *Annales de Geophysique*, *20*(3), 349–364. https://doi.org/10.5194/angeo-20-349-2002

Chen, L., Thorne, R. M., Jordanova, V. K., & Horne, R. B. (2010). Global simulation of magnetosonic wave instability in the storm time magnetosphere. *Journal of Geophysical Research*, *115*, A11222. https://doi.org/10.1029/2010JA015707

Chen, L., Thorne, R. M., Jordanova, V. K., Thomsen, M. F., & Horne, R. B. (2011). Magnetosonic wave instability analysis for proton ring distributions observed by the LANL magnetospheric plasma analyzer. *Journal of Geophysical Research*, *116*, A03223. https://doi.org/10.1029/2010JA016068

Denton, R. E., Engebretson, M. J., Keiling, A., Walsh, A. P., Gary, S. P., Décréau, P. M. E., … Rème, H. (2010). Multiple harmonic ULF waves in the plasma sheet boundary layer: Instability analysis. *Journal of Geophysical Research*, *115*, A12224. https://doi.org/10.1029/2010JA015928

Fernandes, P. A., Larsen, B. A., Thomsen, M. F., Skoug, R. M., Reeves, G. D., Denton, M. H., … Olson, D. K. (2017). The plasma environment inside geostationary orbit: A Van Allen Probes HOPE survey. *Journal of Geophysical Research: Space Physics*, *122*, 9207–9227. https://doi.org/10.1002/2017JA024160

Ferradas, C. P., Zhang, J.-C., Spence, H. E., Kistler, L. M., Larsen, B. A., Reeves, G., … Funsten, H. (2016). Ion nose spectral structures observed by the Van Allen Probes. *Journal of Geophysical Research: Space Physics*, *121*, 12,025–12,046. https://doi.org/10.1002/2016JA022942

Gary, S. P., & Lee, M. A. (1994). The ion cyclotron anisotropy instability and the inverse correlation between proton anisotropy and proton beta. *Journal of Geophysical Research*, *99*(A6), 11,297–11,301. https://doi.org/10.1029/94JA00253

Gary, S. P., Liu, K., & Winske, D. (2011). Bernstein instability driven by suprathermal protons in the ring current. *Journal of Geophysical Research*, *116*, A08215. https://doi.org/10.1029/2011JA016543

Gary, S. P., Liu, K., Winske, D., & Denton, R. E. (2010). Ion Bernstein instability in the terrestrial magnetosphere: Linear dispersion theory. *Journal of Geophysical Research*, *115*, A12209. https://doi.org/10.1029/2010JA015965

Gary, S. P., Moldwin, M. B., Thomsen, M. F., Winske, D., & McComas, D. J. (1994). Hot proton anisotropies and cool proton temperatures in the outer magnetosphere. *Journal of Geophysical Research*, *99*(A12), 23,603–23,615. https://doi.org/10.1029/94JA02069

Gary, S. P., Wang, J., Winske, D., & Fuselier, S. A. (1997). Proton temperature anisotropy upper bound. *Journal of Geophysical Research*, *102*(A12), 27,159–27,169. https://doi.org/10.1029/97JA01726

Gurnett, D. A. (1976). Plasma wave interactions with energetic ions near the magnetic equator. *Journal of Geophysical Research*, *81*(16), 2765–2770. https://doi.org/10.1029/JA081i016p02765

Hamlin, D. A., Karplus, R., Vik, R. C., & Watson, K. M. (1961). Mirror and azimuthal drift frequencies for geomagnetically trapped particles. *Journal of Geophysical Research*, *66*(1), 1–4. https://doi.org/10.1029/JZ066i001p00001

Horne, R. B., & Thorne, R. M. (1998). Potential waves for relativistic electron scattering and stochastic acceleration during magnetic storms. *Journal of Geophysical Research*, *25*(15), 3011–3014. https://doi.org/10.1029/98GL01002

Horne, R. B., Thorne, R. M., Glauert, S. A., Meredith, N. P., Pokhotelov, D., & Santolík, O. (2007). Electron acceleration in the Van Allen radiation belts by fast magnetosonic waves. *Geophysical Research Letters*, *34*, L17107. https://doi.org/10.1029/2007GL030267

Horne, R. B., Wheeler, G. V., & Alleyne, H. S. C. K. (2000). Proton and electron heating by radially propagating fast magnetosonic waves. *Journal of Geophysical Research*, *105*(A12), 27,597–27,610. https://doi.org/10.1029/2000JA000018

Kasahara, Y., Kenmochi, H., & Kimura, I. (1994). Propagation characteristics of the ELF emissions observed by the satellite Akebono in the magnetic equatorial region. *Radio Science*, *29*(4), 751–767. https://doi.org/10.1029/94RS00445

Kistler, L. M., Ipavich, F. M., Hamilton, D. C., Gloeckler, G., Wlken, B., Kremser, G., & Stüdemann, W. (1989). Energy spectra of the major ion species in the ring current during geomagnetic storms. *Journal of Geophysical Research*, *94*(A4), 3579–3599. https://doi.org/10.1029/JA094iA04p03579

Kovrazhkin, R. A., Sauvaud, J. A., & Delcourt, D. C. (1999). INTERBALL-Auroral observations of 0.1–12 keV ion gaps in the diffuse auroral zone. *Annales de Geophysique*, *17*, 734–742.

Laakso, H., Junginger, H., Roux, A., Schmidt, R., & de Villedary, C. (1990). Magnetosonic waves above *fc* (H+) at geostationary orbit: GEOS2 results. *Journal of Geophysical Research*, *95*(A7), 10,609–10,621. https://doi.org/10.1029/JA095iA07p10609

Liu, K., Gary, S. P., & Winske, D. (2011). Excitation of magnetosonic waves in the terrestrial magnetosphere: Particle-in-cell simulations. *Journal of Geophysical Research*, *116*, A07212. https://doi.org/10.1029/2010JA016372

Ma, Q., Li, W., Chen, L., Thorne, R. M., & Angelopoulos, V. (2014). Magnetosonic wave excitation by ion ring distributions in the Earth's inner magnetosphere. *Journal of Geophysical Research: Space Physics*, *119*, 844–852. https://doi.org/10.1002/2013JA019591

Ma, Q., Li, W., Thorne, R. M., & Angelopoulos, V. (2013). Global distribution of equatorial magnetosonic waves observed by THEMIS. *Geophysical Research Letters*, *40*, 1895–1901. https://doi.org/10.1002/grl.50434

McClements, K. G., Dendy, R. O., & Lashmore-Davies, C. N. (1994). A model for the generation of obliquely propagating ULF waves near the magnetic equator. *Journal of Geophysical Research*, *99*(A12), 23,685–23,693. https://doi.org/10.1029/94JA01979

Min, K., & Liu, K. (2015). Fast magnetosonic waves driven by shell velocity distributions. *Journal of Geophysical Research: Space Physics*, *120*, 2739–2753. https://doi.org/10.1002/(ISSN)2169-9402

Min, K., & Liu, K. (2016). Proton velocity ring-driven instabilities in the inner magnetosphere: Linear theory and particle-in-cell simulations. *Journal of Geophysical Research: Space Physics*, *121*, 475–491. https://doi.org/10.1002/2015JA022042

Min, K., Liu, K., & Peter Gary, S. (2016). Scalings of Alfvén-cyclotron and ion Bernstein instabilities on temperature anisotropy of a ring-like velocity distribution in the inner magnetosphere. *Journal of Geophysical Research: Space Physics*, *121*, 2185–2193. https://doi.org/10.1002/2015JA022134

Perraut, S., Roux, A., Robert, P., Gendrin, R., Sauvaud, J.-A., Bosqued, J.-M., … Korth, A. (1982). A systematic study of ULF waves above fH+ from GEOS 1 and 2 measurements and their relationships with proton ring distributions. *Journal of Geophysical Research*, *87*(A8), 6219–6236. https://doi.org/10.1029/JA087iA08p06219

Russell, C. T., Holzer, R. E., & Smith, E. J. (1970). OGO 3 observations of ELF noise in the magnetosphere: 2. The nature of the equatorial noise. *Journal of Geophysical Research*, *75*(4), 755–768. https://doi.org/10.1029/JA075i004p00755

Saikin, A. A., Zhang, J.-C., Smith, C. W., Spence, H. E., Torbert, R. B., & Kletzing, C. A. (2016). The dependence on geomagnetic conditions and solar wind dynamic pressure of the spatial distributions of EMIC waves observed by the Van Allen Probes. *Journal of Geophysical Research: Space Physics*, *121*, 4362–4377. https://doi.org/10.1002/2016JA022523

Thomsen, M. F., Denton, M. H., Jordanova, V. K., Chen, L., & Thorne, R. M. (2011). Free energy to drive equatorial magnetosonic wave instability at geosynchronous orbit. *Journal of Geophysical Research*, *116*, A08220. https://doi.org/10.1029/2011JA016644

Thomsen, M. F., Henderson, M. G., & Jordanova, V. K. (2013). Statistical properties of the surface-charging environment at geosynchronous orbit. *Space Weather*, *11*, 237–244. https://doi.org/10.1002/swe.20049

Thomsen, M. F., Noveroske, E., Borovsky, J. E., & McComas, D. J. (1999). Calculation of moments from measurements by the Los Alamos Magnetospheric Plasma Analyzer. In *Los Alamos Unclassified Report* (Rep. LA-13566-MS). Los Alamos, NM: Los Alamos National Laboratory.

Umeda, T., Matsukiyo, S., Amano, T., & Miyoshi, Y. (2012). A numerical electromagnetic linear dispersion relation for Maxwellian ring-beam velocity distributions. *Physics of Plasmas*, *19*(7), 072107. https://doi.org/10.1063/1.4736848

Xiao, F., Zhou, Q., He, Z., Yang, C., He, Y., & Tang, L. (2013). Magnetosonic wave instability by proton ring distributions: Simultaneous data and modeling. *Journal of Geophysical Research: Space Physics*, *118*, 4053–4058. https://doi.org/10.1002/jgra.50401